Publication Year	2016
Acceptance in OA	2020-06-26T10:24:18Z
Title	GeMS/GSAOI Photometric and Astrometric Performance in Dense Stellar Fields
Authors	Dalessandro, Emanuele, Saracino, S., ORIGLIA, Livia, Marchetti, E., Ferraro, F. R., Lanzoni, B., Geisler, D., Cohen, R. E., Mauro, F., Villanova, S.
Publisher's version (DOI)	10.3847/1538-4357/833/1/111
Handle	http://hdl.handle.net/20.500.12386/26227
Journal	THE ASTROPHYSICAL JOURNAL
Volume	833

The Astrophysical Journal, 833:111 (18pp), 2016 December 10
doi:10.3847/1538-4357/833/1/111

GeMS/GSAOI PHOTOMETRIC AND ASTROMETRIC PERFORMANCE IN DENSE STELLAR FIELDS

E. Dalessandro[1,2], S. Saracino[1,2], L. Origlia[1], E. Marchetti[3], F. R. Ferraro[2], B. Lanzoni[2], D. Geisler[4], R. E. Cohen[4], F. Mauro[4,5], and S. Villanova[4]
[1] INAF—Osservatorio Astronomico di Bologna, via Ranzani 1, I-40127, Bologna, Italy
[2] Dipartimento di Fisica & Astronomia, Università degli Studi di Bologna, viale Berti Pichat 6/2, I-40127 Bologna, Italy
[3] ESO—European Southern Observatory, Karl Schwarzschild Str. 2, D-85748 Garching bei Muenchen, Germany
[4] Departamento de Astronomía, Universidad de Concepción, Casilla 160-C, Concepción, Chile
[5] Millennium Institute of Astrophysics, Chile
Received 2016 August 4; revised 2016 September 19; accepted 2016 October 6; published 2016 December 12

ABSTRACT

Ground-based imagers at 8 m class telescopes assisted by multi-conjugate adaptive optics are primary facilities with which to obtain accurate photometry and proper motions in dense stellar fields. We observed the central region of the globular clusters Liller 1 and NGC 6624 with the Gemini Multi-conjugate Adaptive Optics System (GeMS) feeding the Gemini South Adaptive Optics Imager (GSAOI) currently available at the Gemini South telescope, under different observing conditions. We characterized the stellar point-spread function (PSF) in terms of FWHM, Strehl ratio (SR), and encircled energy (EE), over the field of view (FOV). We found that, for sub-arcsecond seeing at the observed airmass, we can obtain the diffraction-limited PSF (FWHM $\approx$80 mas), SR $\sim$ 40%, and EE $\geqslant$ 50% with a dispersion around 10% over the FOV of $85'' \times 85''$, in the K_s band. In the J band the best images provide FWHMs between 60 and 80 mas, SR $>$10%, and EE $>$ 40%. For seeing at the observed airmass exceeding $1''$, the performance worsens but it is still possible to perform PSF fitting photometry with 25% EE in J and 40% in K_s. We also computed the geometric distortions of GeMS/GSAOI and we obtained corrected images with an astrometric accuracy of $\sim$1 mas in a stellar field with high crowding.

Key words: astrometry – instrumentation: adaptive optics – instrumentation: high angular resolution – stars: imaging – techniques: photometric – telescopes

1. INTRODUCTION

Adaptive optics (AO) systems sample and correct in real time the wavefront deformation due to atmospheric turbulence, which affects the overall sharpness and spatial resolution of astronomical images obtained with ground-based telescopes.

The first AO systems were based on a single guide star, either the target itself if bright enough, or a bright star within a few arcseconds of the astronomical target. This system, called single-conjugate AO (SCAO), however, only partially corrects the atmospheric turbulence because of the anisoplanatism, with best correction on axis and a blurring size of the astronomical image that increases with increasing distance from the guide star.

In order to increase the field of view (FOV) with good AO corrections, it is necessary to use multiple guide stars and correct for multiple layers of turbulence in the atmosphere. Ground-based near-IR (NIR) imagers assisted by multi-conjugate AO (MCAO) systems represent the technological frontier of the last decade in obtaining high-quality stellar photometry in crowded fields at the highest possible spatial resolution, by reaching the diffraction limit of 8 m class telescopes.

The advantage of using an MCAO over SCAO is significant: while normally the latter provides a Strehl ratio (SR) above 20% within $20''$ of the guide star, with an MCAO system one can obtain such SRs over a FOV as large as a few arcminutes (Beckers 1988; Ellerbroek et al. 1994; Johnston & Welsh 1994; Le Louarn 2002; Marchetti et al. 2007).

The first MCAO system used for nighttime astronomical observations was the Multi-conjugate Adaptive-optics Demonstrator (MAD) operating at the Very Large Telescope (VLT) in 2007–2008 (Marchetti et al. 2007). MAD used up to three natural guide stars (NGSs) for the wavefront sensing, and tip–tilt correction and two deformable mirrors conjugated at the ground and at an altitude of 8.5 km, providing a corrected FOV of about $1' \times 1'$. A few works on stellar photometry in the dense stellar fields of Galactic globular clusters (see, e.g., Ferraro et al. 2009; Moretti et al. 2009; Bono et al. 2010; Ortolani et al. 2011) have shown how effective an MCAO system such as MAD could be in providing uniform point-spread functions (PSFs) and accurate photometry across the entire FOV of $1' \times 1'$.

Since 2013 the Gemini Multi-conjugate Adaptive Optics System (GeMS) together with the Gemini South Adaptive Optics Imager (GSAOI) at the Gemini South telescope (Rigaut et al. 2012, 2014; Neichel et al. 2014a, 2014b) has regularly been offered to the community for observations. This is the only MCAO facility currently at work in the world. GeMS is the first sodium-based multi-laser MCAO system. It uses five lasers and three tip–tilt stars to provide an efficient correction over a FOV of $\sim 1'.5 \times 1'.5$. GSAOI is an NIR imager equipped with four 2k × 2k detectors with pixel size 20 mas, covering $85'' \times 85''$, and designed to work at the diffraction limit of an 8 m telescope.

The proper characterization of the image quality delivered by the GeMS/GSAOI system and of the parameters that mostly contribute to setting its overall efficiency is extremely important in deciding the best observational strategy and maximizing the scientific output. It also provides useful information for the future generation of MCAO systems at the 20–40 m class giant telescopes currently in development.

Indeed, various authors have put significant effort into this task. In particular, Neichel et al. (2014b; see also Rigaut et al. 2012, 2014; Vidal et al. 2013) have analyzed the average performance of GeMS in terms of variations in SR and FWHM

Table 1
Properties of the Data Set

Cluster	Date	Number of J exposures	Number of K_s exposures	$\langle s(500\ \mathrm{nm})\rangle$	$\langle\mathrm{airmass}\rangle$
Liller 1	2013 Apr 20	3	10	1.07	1.03
Liller 1	2013 May 22	0	5	1.05	1.44
Liller 1	2013 May 24	9	0	0.75	1.018
NGC 6624	2013 May 24	13	14	0.66	1.02

Note. Average seeing values at zenith, s(500 nm), are in arcseconds.

for a large sample of images acquired during the Science Verification. They find that, with a median seeing of 0.″73, the average FWHM delivered by the system for 50% of the images is 0.″087, 0.″075, and 0.″095 in the J, H, and K_s bands, respectively. For reference, the diffraction-limited FWHMs are, e.g., 0.″037, 0.″049, and 0.″068 at 1.2, 1.6, and 2.2 μm, respectively. They also find that the average variation in FWHM over a field of one square arcminute is ~5% (relative rms), with the maximum variation being ~15%. For the same images the average SR is 5% in J and 17% in K_s. More generally, the SR and FWHM can vary by a factor of 2–3 (also depending on the filter considered) for a variation in seeing in the range 0.″5–1.″5.

In addition to the natural seeing, there are other physical parameters that can affect the performance of the GeMS/GSAOI and AO systems in general. Among them, a non-negligible role is played by the brightness and asterism of the NGSs, the photon return of the laser guide star (LGS), the speed of turbulence, and its profile. In particular, Vidal et al. (2013) and Neichel et al. (2014b) have shown that the seasonal change of the LGS photon return can affect the delivered average FHWM and SR values by up to a factor of 2–3. Along the same lines, Vidal et al. (2013) illustrate a case where for the same targets, same photon return, and natural seeing, the SR drops by a factor of two, most likely due to variations in the profile of atmospheric turbulence (C_N^2).

These works clearly demonstrate the importance and complexity of disentangling the impact of different factors on the final performance of the AO system. Following these first characterizations, we present here a complementary analysis with the aim of looking at the GeMS/GSAOI performance from an observer/user perspective and providing additional information to be eventually used for Phase I and Phase II preparation. To this aim, we use a sample of images acquired within a scientific proposal devoted to the study of the properties and stellar content of a sample of globular clusters in the Galactic bulge. First results from this project have recently been published by Saracino et al. (2015, 2016).

In addition to the average values of FWHM and SR that have also been analyzed in previous papers, we examine the behavior of the encircled energy (EE) as a function of natural seeing. This quantity is a very intuitive parameter characterizing the properties of the PSF, and it can be directly compared to diffraction-limited space telescopes as well as ground-based instruments not supported by AO facilities. We also add a systematic analysis of how natural seeing impacts the uniformity of the PSF. For the first time we tentatively take account of the role played by the airmass and NGS brightness and we present the first analytic solution for the geometric distortions (GDs) of the GeMS/GSAOI system.

The paper is structured as follows: in Section 2 we describe the data set and data analysis; in Section 3 we provide a characterization of the GeMS/GSAOI performance by using the FWHM of the PSF, the SR, and EE as figures of merit, and a comparison with *Hubble Space Telescope* (*HST*) images; in Section 4 we analyze the GDs; and in Section 5 we draw our conclusions.

2. DATA SET AND OBSERVING CONDITIONS

By using GeMS/GSAOI we observed the central regions of two globular clusters in the Galactic bulge, Liller 1 and NGC 6624, between 2013 April and 2013 May (Program ID: GS-2013A-Q-23; PI: D. Geisler). Two different sets of J and K_s images for Liller 1 and one set for NGC 6624 (see Table 1) have been acquired using an exposure time of 30 s for each individual acquisition.

Each image has been sky-subtracted and flat-field-corrected by using suitable master sky and dome flat frames in the J and K_s filters. We recall that each image is actually a mosaic of four chips that have been reduced and calibrated independently.

The atmospheric seeing at the zenith and at a given wavelength λ can be computed using the formula: $s(\lambda) = \lambda/R_0(\lambda)$. We used the Fried parameter R_0 at $\lambda = 500$ nm and at the zenith reported in each image header to obtain $s(500\ \mathrm{nm}) = 10.31/R_0(500\ \mathrm{nm})$, where R_0 is in units of cm and the seeing in units of arcseconds.

However, it is eventually useful to compute the seeing at the sky position of the target (i.e., at the observing airmass). We thus used the formula $s(\lambda, z) = \lambda/(R_0(\lambda) \times \sec z^{-3/5})$ to obtain $s(500\ \mathrm{nm}, z) = 10.31/(R_0(500\ \mathrm{nm}) \times \sec z^{-3/5})$. Seeing can be computed at other reference wavelengths by using the scaling relation $s(\lambda)/s(500\ \mathrm{nm}) = (\lambda/500\ \mathrm{nm})^{-0.2}$. Hereafter, we always refer to seeing at 500 nm.

It turns out that our images have been acquired under significantly different atmospheric conditions, with seeing $s(500\ \mathrm{nm})$ varying from ~0.″5 to ~1.″5. In particular, the data on NGC 6624 have been obtained with an average value of $s(500\ \mathrm{nm}) \sim 0.''65$, while those for Liller 1 have been obtained under worse conditions with $s(500\ \mathrm{nm}) \sim 1.''00$.

Three reference guide stars in each cluster (see Table 2) have been selected for the tip–tilt correction. The guide stars of NGC 6624 are likely cluster members that are luminous and cool giants near the tip of the red giant branch with fmag $\sim R = 13$–14. The guide stars in Liller 1 are likely blue foreground stars, with significantly fainter J, H, K_s magnitudes and similar fmag ~ R-band magnitudes compared to those of NGC 6624, with the exception of NGS 1, which is a couple of magnitudes fainter. Since the R-band is the spectral range where the wavefront is mostly sensed, this may have some relevance in the final performance (see Section 3.1).

Table 2
Selected Tip–Tilt Guide Stars

Star	K_s	H	J	I	V	R	fmag
Liller 1							
NGS 1 (2MASS J17332197-3323043)	12.799	12.715	12.958	···	···	···	15.338
NGS 2 (2MASS J17332484-3322502)	11.127	11.185	11.418	···	···	···	13.947
NGS 3 (2MASS J17332609-3323129)	11.297	11.074	11.735	···	···	···	13.577
NGC 6624							
NGS 1 (2MASS J18233752-3022018)	8.472	8.723	9.730	11.3850	13.4520	13.094	13.793
NGS 2 (2MASS J18234108-3022221)	8.987	9.202	10.100	11.6230	12.9890	13.219	13.662
NGS 3 (2MASS J18234052-3021392)	8.827	9.274	9.899	12.8800	14.1040	13.776	10.889

Note. Identification name and K_s, H, J magnitudes from 2MASS, V, I from Sarajedini et al. (2007), R estimated from isochrones, fmag (in the spectral range 579–642 nm) from the UCAC3 catalog.

To quantify how the LGS photon return changed during the observing nights, we use the photon counts from the LGS wavefront sensor reported in the header of each image. First, it is important to stress here that the images analyzed in this paper have mostly been acquired over two nights separated by a relatively short time interval (see Table 1), while the LGS photon return is expected to vary mostly seasonally (Vidal et al. 2013; Neichel et al. 2014b). Also, about half of the images of Liller 1 were obtained on the same night as those of NGC 6624 (2013 May 24). As expected, we find a negligible variation in the average photon counts of the LGS during the observing nights.

3. OVERALL PERFORMANCE

We used the IDL-based `Multi-Strehl Meter` software written by E. Marchetti (Marchetti et al. 2006) to analyze the PSF of the science images and measure their FWHM, SR, and EE with variable observing conditions, in order to characterize the performance of the AO system over a range of conditions.

The first step of the analysis is the identification of the candidate star peaks. The software requires as input parameters a first-guess FWHM, the detection threshold, and the size of the subimage to search for the star peaks and to compute the local (residual) background. The first-guess FWHM has been determined by computing the average FWHM of a number of reference stars selected manually on each image. A detection threshold of 1000 ADU and a subimage size of 60 pixels have been used. Moreover, the software requires a few additional input parameters, among them the reference wavelength (1.25 and 2.15 μm for the J and K_s filters, respectively), the pixel size (20 mas), the telescope aperture (8.1 m), and the obstruction factor of the primary mirror (12.35%).

The obtained list of candidate stellar peaks for each image, suitably filtered by spurious detections, has then been cross-correlated with the photometric catalogs containing calibrated magnitudes and astrometric positions published by Saracino et al. (2015) for Liller 1 and Saracino et al. (2016) for NGC 6624, in order to deliver the final list of stars to be analyzed. Typically about 200 stars distributed homogeneously in the FOV in each image have been selected and their FWHM, SR, and EE have been measured. The EE has been computed within a circular aperture of twice the measured FWHM, i.e., the typical aperture adopted in the photometric analysis.[6]

We then computed average and corresponding dispersion values of the FWHM, SR, and EE in each observed image and we analyzed their trends as a function of the seeing at the zenith (s(500 nm), see Figures 1 and 3) and at the observing airmass (s(500 nm, z), see Figures 2 and 4).

3.1. PSF Average Properties

As shown in the left panels of Figure 1, in the K_s band average FWHMs very close to the diffraction limit of 70 mas, SR of ~40%, and EE of 55% have been measured in the NGC 6624 images with sub-arcsecond seeing and airmass close to one. In the Liller 1 images with seeing between 0.″9 and 1.″5, the average FWHM, SR, and EE show a clear trend with the seeing but also quite a large scatter at a given seeing. As seeing at the observing airmass increases from 0.″9 to 1.″5, FWHM increases from 85 to 140 mas, while SR drops from 30% to 12% and EE from 50% to 40%. The general observed trend, as well as the total range of values derived for NGC 6624 and Liller 1 in terms of both FWHM and SR, is consistent with that found by Vidal et al. (2013) and Neichel et al. (2014b) for K_s images. It is interesting to note that the largest average FWHM and the lowest SR and EE for a given seeing are measured in those images acquired at the largest airmass, corresponding to ~1.4. Hence, as shown in the left panels of Figure 2, when the FWHM, SR, and EE are plotted against the seeing at the observing airmass, the scatter is reduced. These measurements and comparisons indicate that the airmass also has an impact on the delivered performance, and in this respect it is worth noting that different observing airmasses could indeed explain some of the scatter observed in Figure 6 of Neichel et al. (2014b), where their measured FWHMs and SRs are plotted against seeing at the zenith.

Most of the J-band images have been acquired at airmass close to one, hence their seeing at the observing airmass is very similar to the seeing at the zenith. As shown in the right panels of Figures 1 and 2 the average FWHMs always exceed the diffraction limit of 40 mas, even with good seeing conditions of 0.″6, and they increase almost linearly with increasing seeing. The corresponding average SR and EE values decrease with increasing seeing. As seeing increases from 0.″6 to 1.″2, FWHM increases from 70 mas to 120 mas, while SR drops from 15% to a few per cent and EE from 40% to 25%. Our FWHM and SR values indicate somewhat better performance of GeMS/GSAOI in the J band than in the findings by Vidal et al. (2013) and Neichel et al. (2014b), likely because of the uniform and good atmospheric conditions during our observations.

---

[6] The Multi-Strehl Meter software actually yields the ensquared energy within twice the FWHM. We then rescaled such a quantity to a circular aperture having the corresponding diameter.

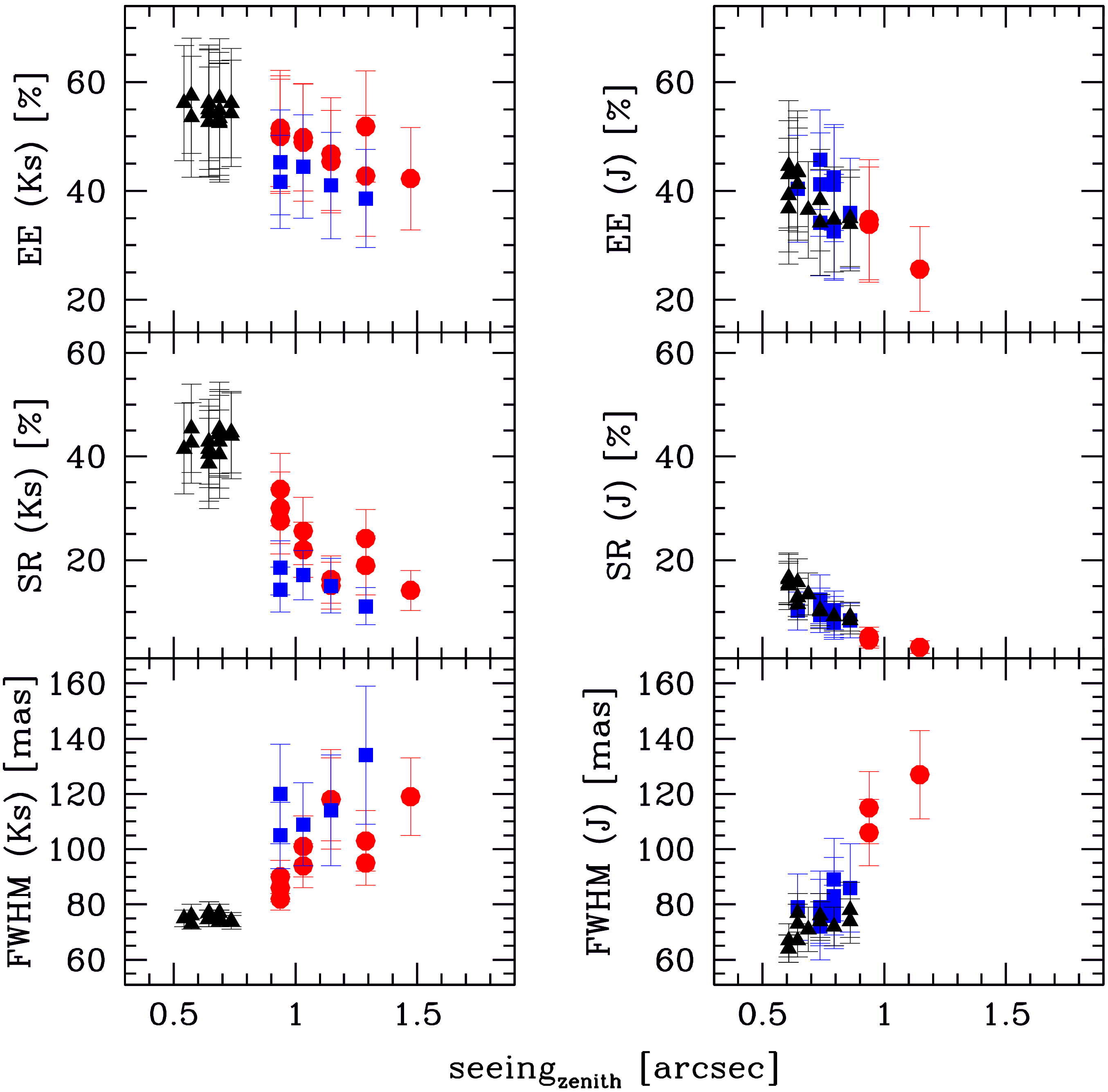

Figure 1. Average FWHM, SR, and EE values with varying seeing at 500 nm at the zenith. Left panels: measurements in the K_s band, right panels: measurements in the J band. Triangles refer to measurements of stars in NGC 6624; circles and squares refer to measurements of stars in Liller 1 observed on two different nights, respectively (see Table 1).

A subsample of images in the J band of Liller 1 and NGC 6624 have been acquired with the same seeing, between 0.″6 and 0.″9, and can be used to check the impact of the different asterisms of the two clusters, and in particular the fact that one guide star in Liller 1 has a significantly fainter R-band magnitude (see Table 2). On average, the Liller 1 images show a ~10%–15% larger FWHM and smaller SR values, which could indeed be a consequence of the significantly fainter guide star.

Finally, we note that in both the K_s and J bands, the average EE values show a smoother variation with seeing when compared to the variation in the FWHM and SR parameters. This is somewhat expected, given that the EE is computed within a variable aperture, proportional to the variable FWHM, and it indicates that the seeing primarily impacts the spatial resolution (i.e., the FWHM and the SR) and to a lesser extent the photometric signal (i.e., the EE), when computed via variable PSF fitting.

3.2. PSF Uniformity

The average values of the FWHM, SR, and EE provide a measurement of the system efficiency, while their dispersion and spatial variation provide an estimate of the uniformity of the PSF across the FOV. Modeling the PSF variations within the FOV is one of the major issues in the photometric analysis

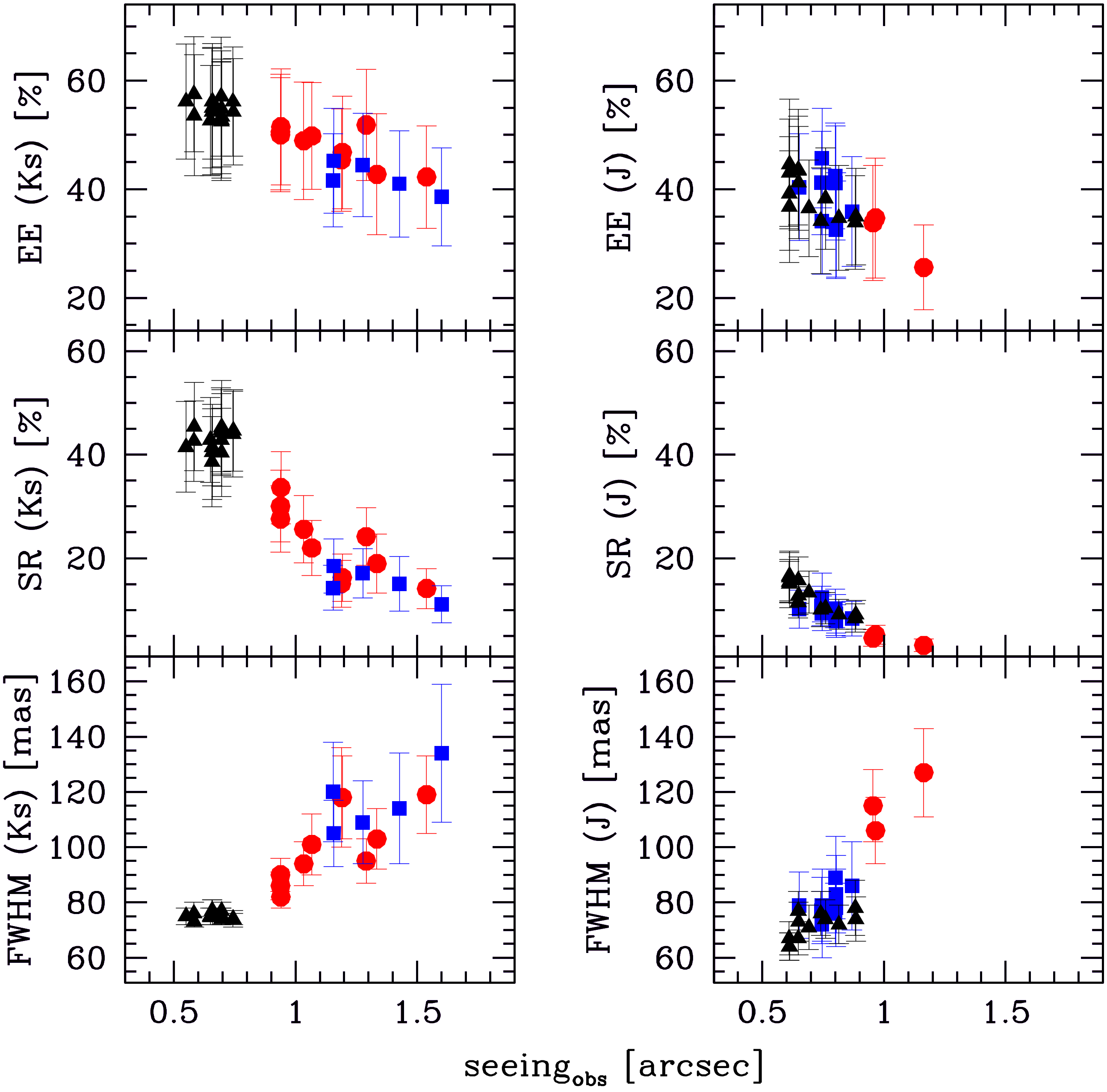

Figure 2. Same as in Figure 1, but for seeing at 500 nm at the observing airmass.

of crowded stellar fields in general, and especially when observed with ground-based AO-assisted imagers. Typical values of FWHM and SR variations can be found in the literature; in the following we quantify how their amplitudes vary as a function of the observing conditions.

As shown in Figures 3 and 4, the dispersion around the average FWHM increases with increasing seeing in a similar fashion to the FWHM itself. This indicates that bad seeing worsens both the spatial resolution and its uniformity over the FOV. In contrast, the dispersion around the average SR and EE decreases with increasing seeing. More uniform SR and EE across the FOV with worsening seeing conditions are somewhat expected. Indeed, in contrast with the FWHM, the SR and the EE are quantities somewhat normalized to the seeing contribution. Hence, when the seeing worsens, its contribution progressively dominates over the diffraction limit peak, and being practically constant across the FOV, it provides a progressively more uniform PSF.

In order to better visualize the spatial variations of the FWHM, SR, and EE, we show in Figures 5 and 6 the maps of their values for three Liller 1 images acquired under different seeing conditions in the K_s and J bands, respectively. The color coding is the same in both figures to allow a direct comparison. As expected, better performance is obtained in better seeing conditions and closer to the guide star asterism, where AO corrections are more efficient, thus yielding smaller values of FWHM and higher values of the SR and EE. It is also interesting to note that the measured counts of the five LGSs, as reported in the headers of the images used, can vary by up to a factor of two, thus possibly contributing to some of the observed gradient.

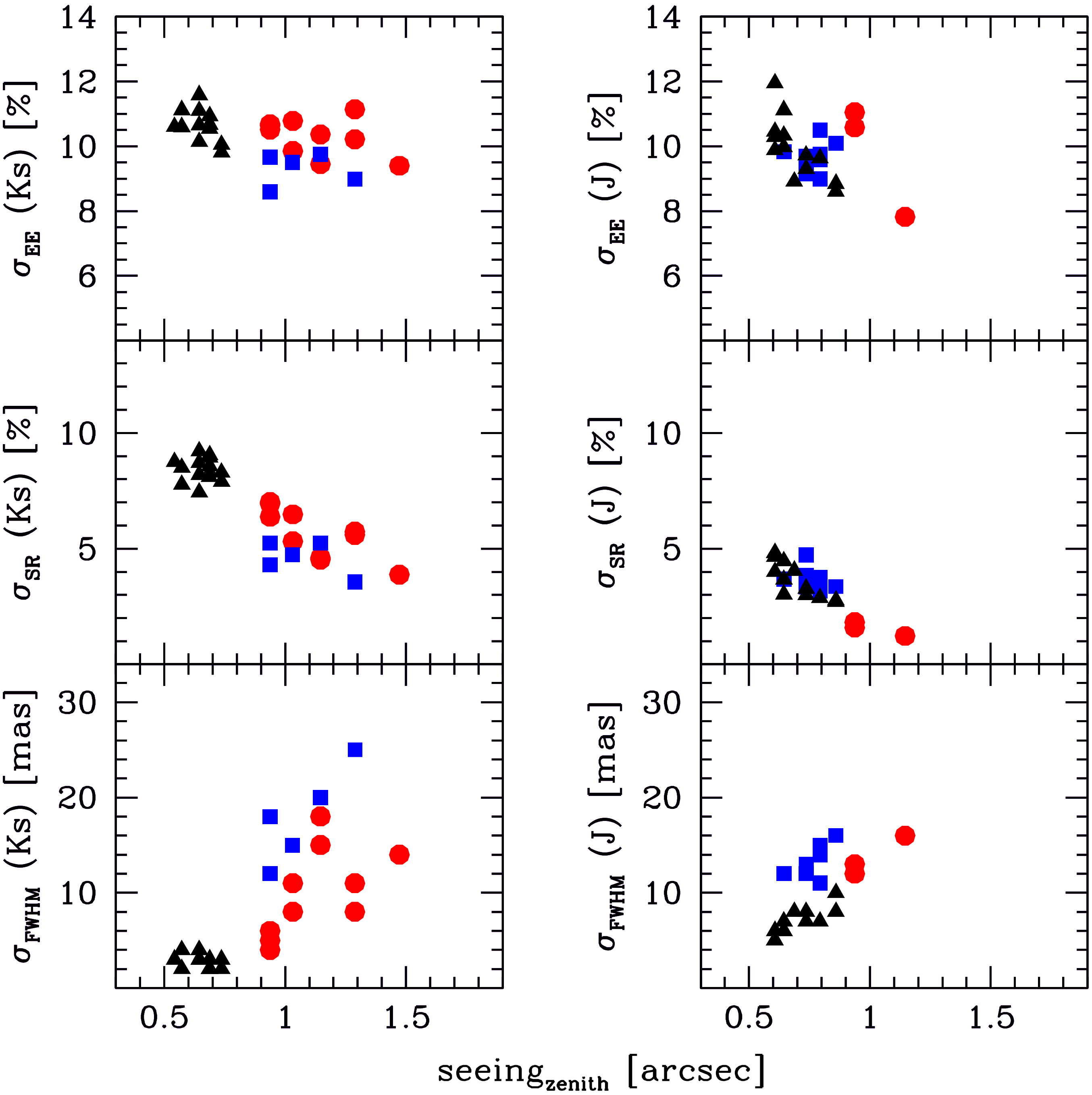

Figure 3. Dispersion around the average FWHM, SR, and EE values with varying seeing at 500 nm at the zenith. Left panels: measurements in the K_s band, right panels: measurements in the J band. Triangles refer to measurements of stars in NGC 6624; circles and squares refer to measurements of stars in Liller 1 as observed on two different nights, respectively (see Table 1).

3.3. GeMS/GSAOI versus HST/ACS Performance

In verifying the potentiality of ground-based MCAO-assisted imagers to obtain accurate photometry in dense stellar fields, it is very interesting to compare the performance of the GeMS/GSAOI system with that of *HST*. However, to perform a meaningful comparison, it is necessary to probe wavelength ranges where similar diffraction limits are expected between the two telescopes. As the primary mirror of *HST* is about three times smaller (~2.4 m) than that of the Gemini South telescope, the diffraction limit expected for Gemini J and K_s images (0.″04–0.″07) is obtained at optical wavelengths with *HST*.

We used two short exposures ($t_{\rm exp} = 15$ s) of NGC 6624 taken with the Advanced Camera for Surveys/Wide Field Camera (ACS/WFC) on board *HST*, in the F606W and F814W bands (Prop: 10775; PI: Sarajedini). A sample of about 200 isolated stars with high signal-to-noise ratio have been selected to compute average FWHM, SR, and EE, and their dispersions around the mean, by using the same analysis as for GeMS/GSAOI images.

We obtain average values of FWHM of 82 and 86 mas for the F606W and F814W bands, respectively. While the average FWHM for F814W is consistent with the nominal diffraction limit of *HST* at these wavelengths (~85 mas), the FWHM in

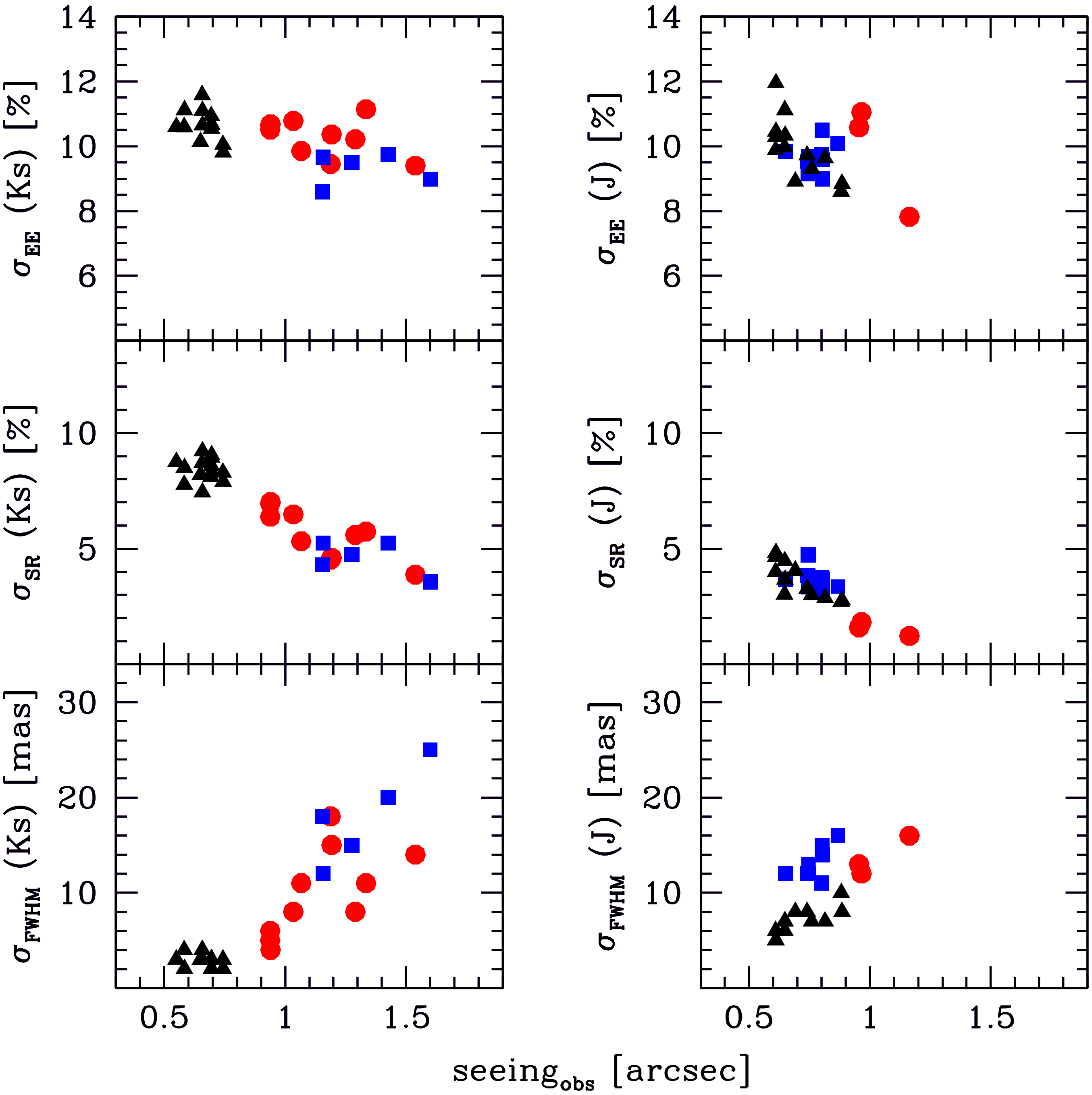

Figure 4. Same as in Figure 3, but for seeing at 500 nm at the observing airmass.

F606W is significantly larger (by ~30%) than the nominal diffraction limit (~63 mas), but this is somewhat expected, since at these wavelengths the limiting factor is the under-sampling of the PSF. We find also that the overall variation of the FWHM across the entire ACS FOV (~200″ × 200″) is ~8%. This value is consistent with a ±10% variation estimated by Anderson (2006) using a significantly larger data set. For the same stars we estimated SR ~ 50% and ~65% for F606W and F814W, respectively, and $\sigma_{SR} < 10\%$ for both filters. Moreover, we find EE ~ 55% and $\sigma_{EE} \sim 10\%$ for both filters. These latter values are consistent with those estimated by Sirianni et al. (2005; Table 3) within a comparable aperture of 2 × FWHM (corresponding to an equivalent circle of radius between 50 and 100 mas) for white-dwarf spectrophotometric standards located at the center of the two ACS/WFC chips.

In Figure 7 we plot the dispersion around the average FWHM, SR, and EE values as a function of the corresponding average values for the GeMS/GSAOI *J* and K_s images, as well as for the *HST*/ACS F606W and F814W ones. For sub-arcsecond seeing conditions, GeMS/GSAOI delivers images with comparable or even better PSF FWHMs than ACS and also similar uniformity over the FOV (at least in the K_s band). In contrast, both the SR and EE are in most cases lower than the corresponding values of ACS, while their variation over the FOV is comparable (around 10%). Only in the best seeing conditions and in the K_s band can GeMS/GSAOI reach EE values comparable to those delivered by *HST*/ACS.

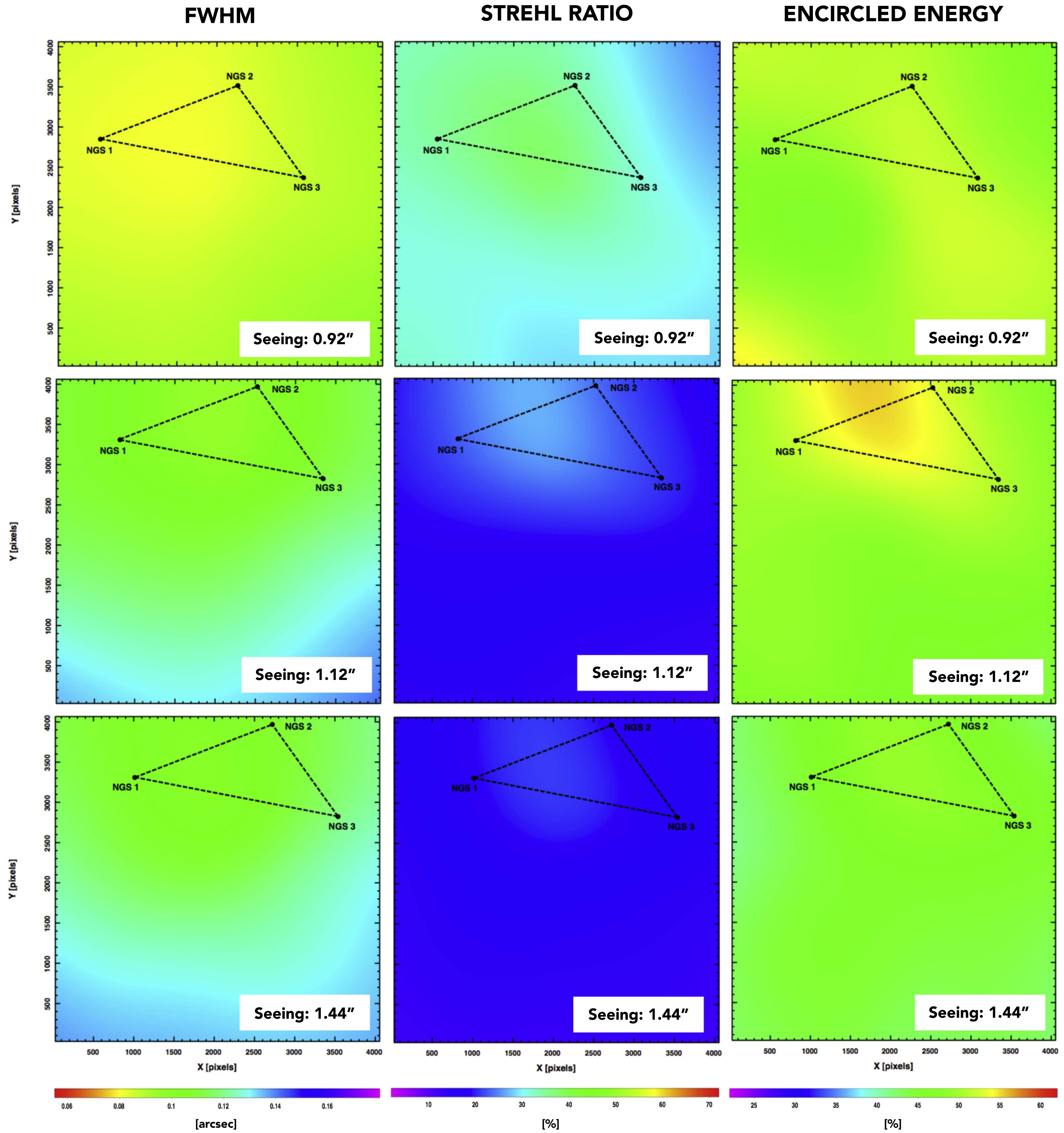

Figure 5. Maps of FWHM (left panels), SR (middle panels), and EE (right panels) for three K_s-band images of Liller 1 acquired under different seeing conditions. The triangle indicates the guide star asterism. The quoted seeing values are at the zenith and at 500 nm. Color coding from magenta (worst) to red (best) is a performance indicator.

In Figure 8 we show the FWHM, SR, and EE maps for three NGC 6624 images in the K_s, J, and F814W filters, respectively. The color coding is the same as in Figures 5 and 6 to allow a direct comparison. As in the case of Liller 1, GeMS/GSAOI delivers better performance (i.e., smaller FWHM and higher SR and EE) in the surroundings of the guide star asterism. *HST*/ACS provides very uniform FWHMs over the entire FOV. SR and EE improve smoothly with increasing radial distance from the center, as expected since crowding decreases. The stars in the very central region of the cluster (white circular area in the bottom panels of Figure 8) were not used to sample the FWHM of the PSF, the SR and EE in the *HST* images, because measurements are quite uncertain due to the prohibitive crowding. However, it was possible to measure them in the GeMS/GSAOI NIR images (the sampled FOV is indicated as a black square in Figure 8), since in that case crowding by resolved stars is less severe than in the *HST* images, due to a combination of a slightly higher spatial resolution and a lower sensitivity to faint stars, which contribute only in the form of unresolved stellar background.

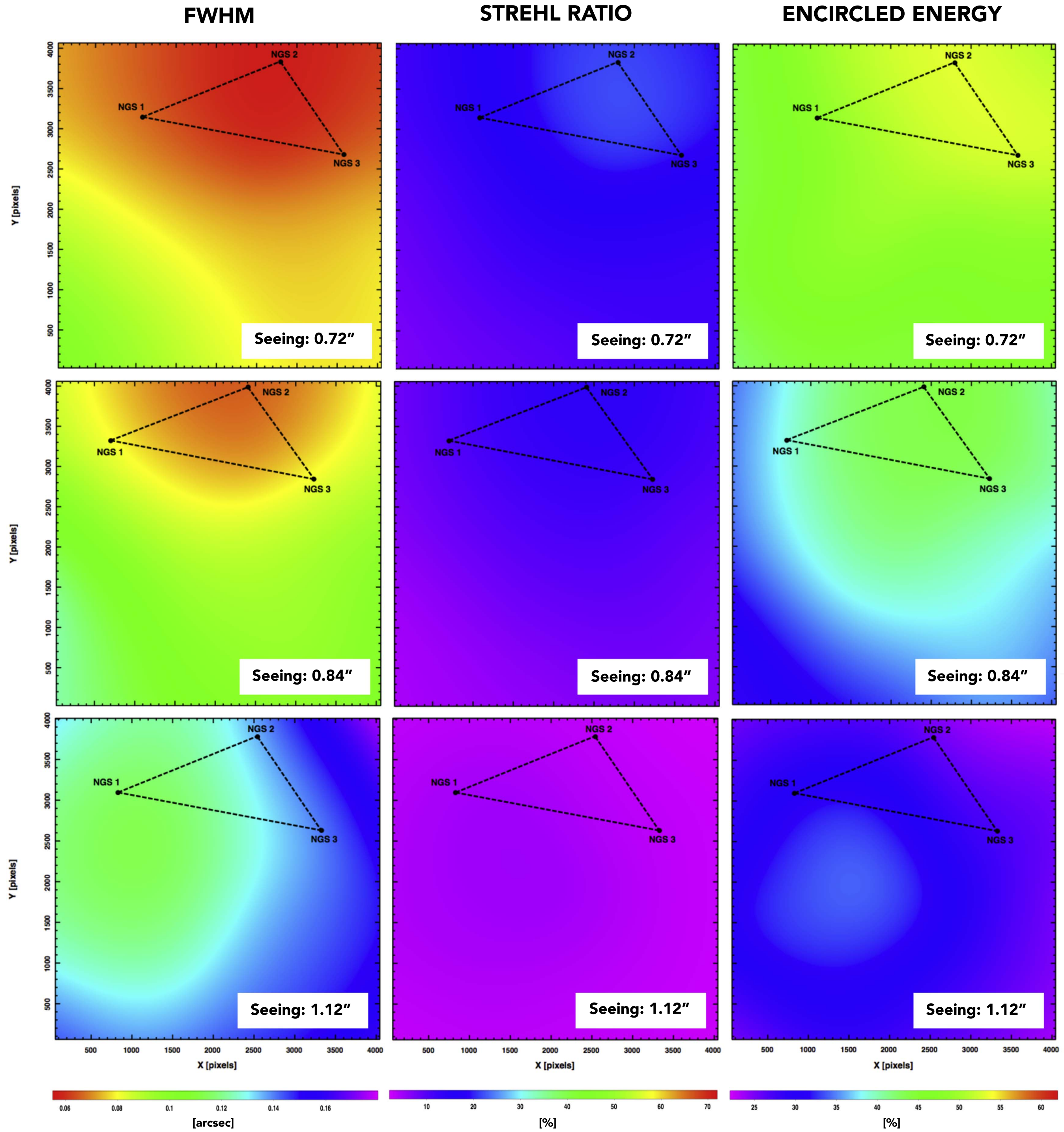

Figure 6. Maps of FWHM (left panels), SR (middle panels), and EE (right panels) for three *J*-band images of Liller 1 acquired under different seeing conditions. The triangle indicates the guide star asterism. The quoted seeing values are at the zenith and at 500 nm. Color coding from magenta (worst) to red (best) is a performance indicator.

4. GeMS/GSAOI ASTROMETRIC PERFORMANCE

High-precision astrometry is crucial for many scientific studies in modern astrophysics. In the study of the stellar populations of globular clusters, precise astrometry is required in order to measure proper motions and obtain precious information on contamination by field stars and on the internal kinematics (see, for example, Richer et al. 2013; Bellini et al. 2015; Watkins et al. 2015). To measure stellar proper motions one needs to derive positional displacements between two (or more) epochs. However, in virtually all available instruments, displacements of stars are not only due to their “real” motions but are also a result of instrumental effects (distortions) that alter the positions of stars artificially and need to be modeled to obtain highly accurate astrometric solutions. In AO-assisted imagers, these distortions are not only of geometric nature, but they can depend also on other factors (such as anisoplanatism), although in the following we will always refer to them as GDs. A successful approach to modeling GDs was proposed for the

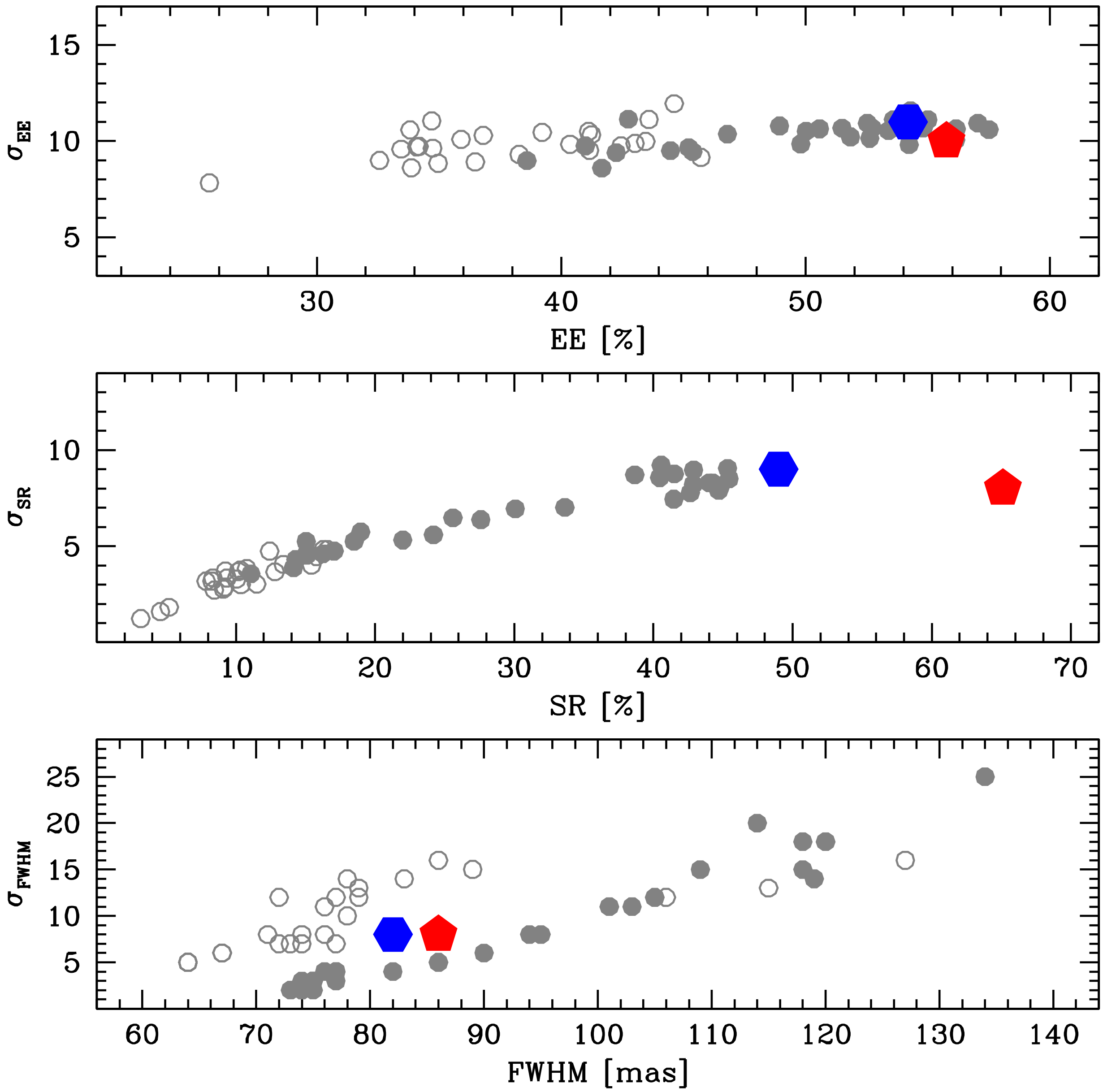

Figure 7. Dispersion around the average FWHM, SR, and EE values as a function of the corresponding average values for the GeMS/GSAOI *J* (open circles) and K_s (filled circles) images, and the *HST*/ACS F606W (hexagon) and F814W (pentagon) ones.

first time by Anderson & King (2003), who found a distortion solution for the *HST* Wide Field Planetary Camera 2. In recent years, other similar works have been published that are aimed at measuring the GD of the ACS and the Wide Field Camera 3 (Bellini & Bedin 2009; Bellini et al. 2011) on board *HST* or of ground-based imagers such as LBT/LBC, ESO/WFI, VLT/HAWK-I, and VISTA/VIRCAM (Anderson et al. 2006; Yadav et al. 2008; Bellini et al. 2009; Bellini & Bedin 2010; Libralato et al. 2014, 2015).

An analysis of the internal astrometric performance of the GeMS/GSAOI system has recently been presented by Neichel et al. (2014a). They find that for single-epoch, well populated, undithered images, an internal astrometric error of ~0.2 mas can be achieved for well exposed images ($t_{\rm exp} > 1$ minute). In contrast, for multi-epoch observations, an additional systematic error of ~0.4 mas should be considered. According to the authors this is likely due to time-variable distortion induced by gravity flexure of the instrument.

In this paper, we attempt to obtain the first formal analytic solution to the GDs of GeMS/GSAOI for the *J* and K_s filters and an analysis of the absolute astrometric performance of the system. To this aim, we closely followed the approach described in Anderson & King (2003) and Bellini & Bedin (2009). We used the single-epoch dithered (by ~3″) images (14 in K_s and 13 in *J*, see Table 1) available for NGC 6624. Indeed this is an ideal data set for this goal for several reasons: (i) during the observing night, the atmospheric conditions were good and quite stable (average seeing ≈0.″65, airmass close to one); (ii) dithering allows both *dynamic* and *static* distortions of the camera to be analyzed (Neichel et al. 2014a); (iii) a distortion-free catalog of the cluster stars to be used as reference is available.

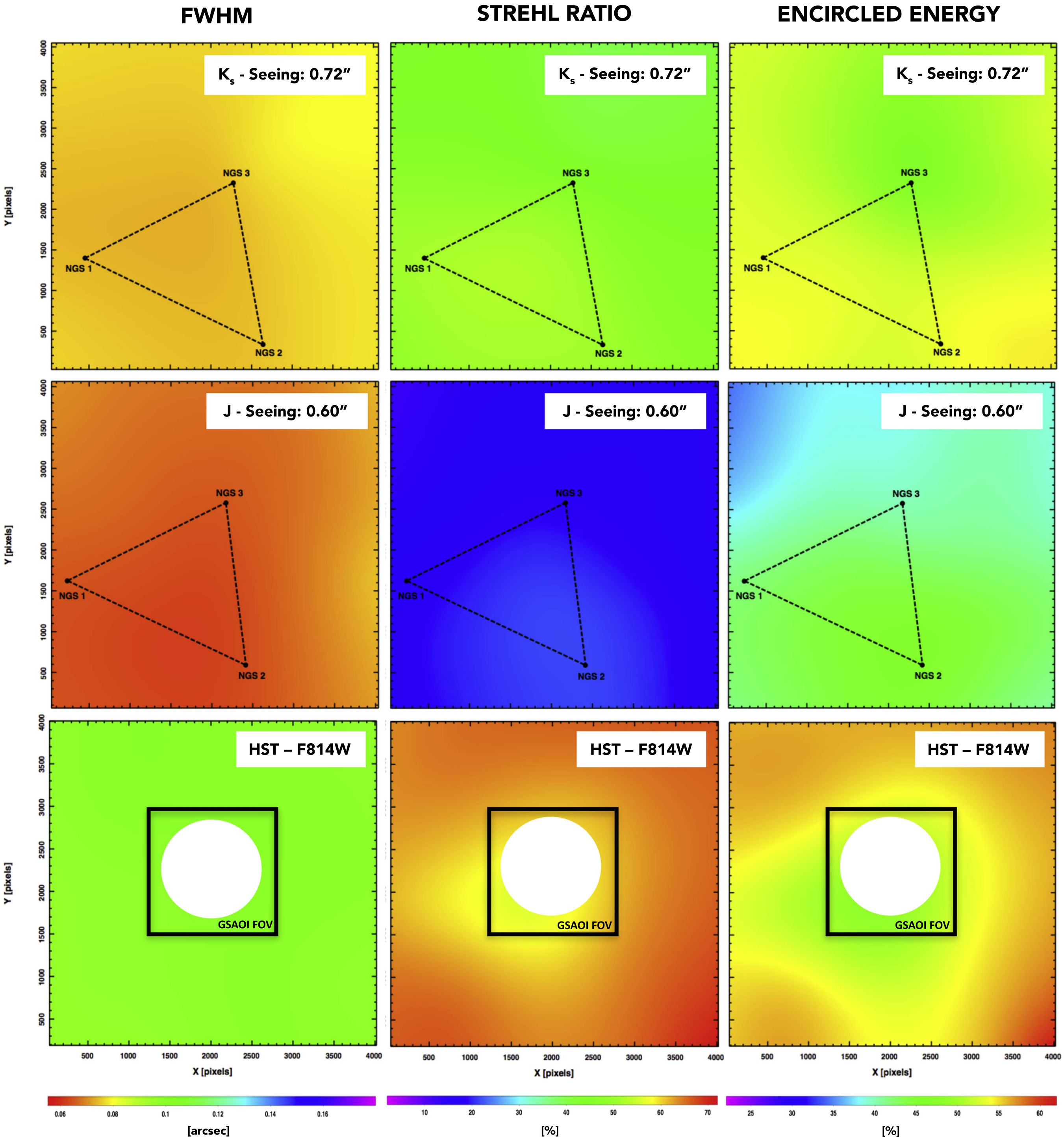

Figure 8. Maps of FWHM (left panels), SR (middle panels), and EE (right panels) for three NGC 6624 images in the K_s (top panels), J (middle panels), and F814W (bottom panels) filters. The triangle indicates the guide star asterism for the GSAOI ground-based images. The central, white area in the *HST* maps was excluded due to the prohibitive crowding, while the black square indicates the GeMS/GSAOI FOV.

4.1. A GD Solution

The most straightforward way to solve for the GD for a given instrument is to compare the positions of stars in that instrument with the corresponding ones in a distortion-free reference catalog, so that information about distortions can be derived directly from the stellar positional residuals. For NGC 6624 we used the ACS catalog published by Sarajedini et al. (2007) as a reference system. In this catalog the positions are corrected for GD effects using the solutions found by Anderson & King (2003) and Meurer et al. (2003). It covers a large enough FOV to entirely include the GeMS/GSAOI data set and it samples the entire magnitude range probed by the GeMS/GSAOI images for NGC 6624.

We combined the ACS catalog with data obtained with the WFC3 UVIS channel within the *HST* UV Legacy Survey of Globular Clusters (Prop: 13297, PI: Piotto; see Piotto et al.

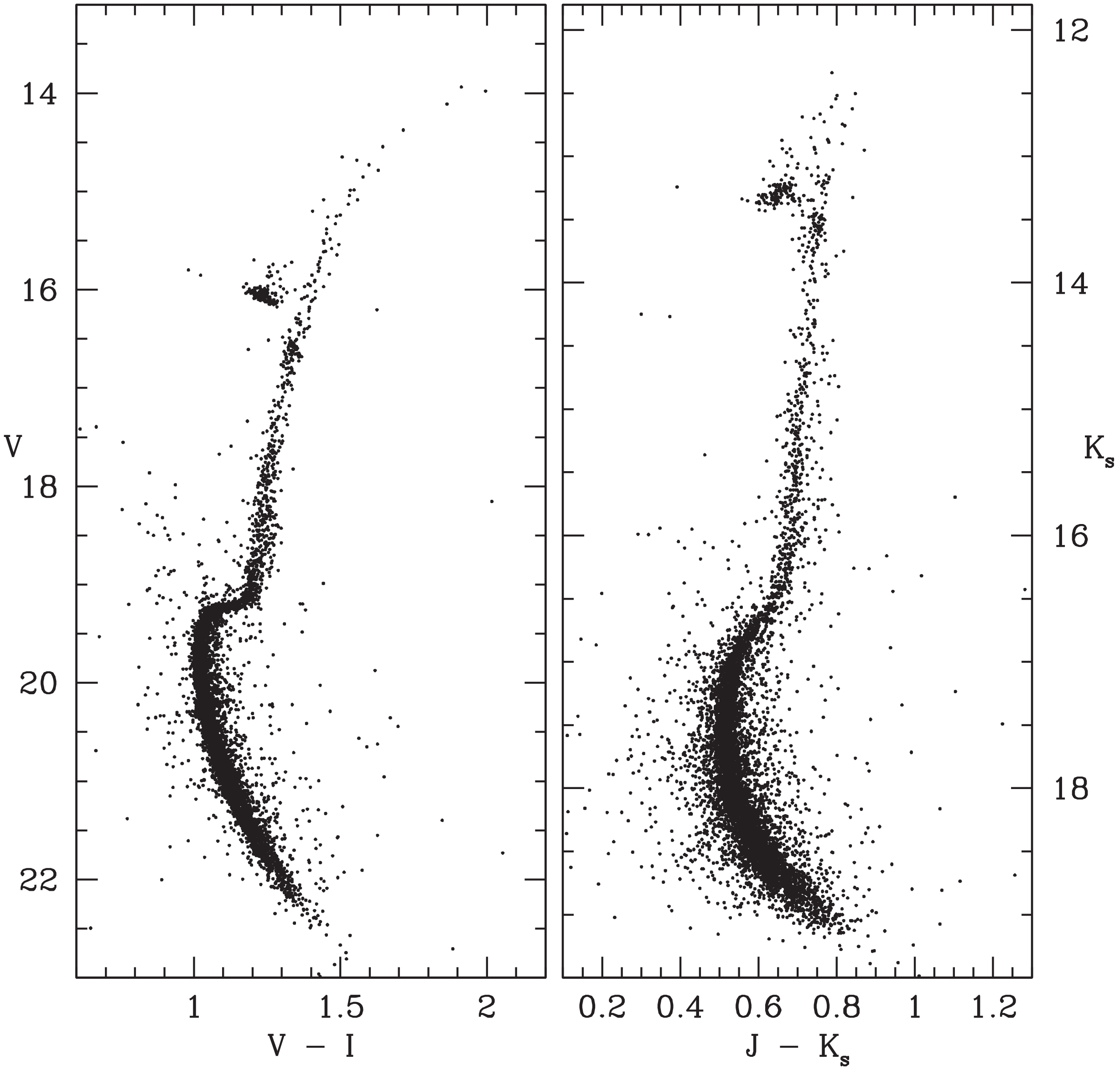

Figure 9. Color–magnitude diagrams (V, $V - I$) (left panel) and (K_s, $J - K_s$) (right panel) of the stars in common between the master catalog and the GeMS/GSAOI catalog of NGC 6624 by Saracino et al. (2016).

Table 3
Coefficients of the Third-order Polynomial for each Chip, Representing the Final GD Solution for the K_s Filter

Term(q)	Polynomial	$a_{q,[1]}$	$b_{q,[1]}$	$a_{q,[2]}$	$b_{q,[2]}$	$a_{q,[3]}$	$b_{q,[3]}$	$a_{q,[4]}$	$b_{q,[4]}$
1	$\tilde{x}$	7.2959	−8.1224	−8.2342	−8.0700	−8.6718	5.5598	7.7150	5.3724
2	$\tilde{y}$	−8.6592	−6.9948	−9.5140	7.0969	5.8746	7.4350	6.7219	−5.4231
3	$\tilde{x}^2$	6.7348	0.0217	7.0562	0.0903	6.9963	0.0301	6.8232	0.1139
4	$\tilde{x}\tilde{y}$	0.1646	−0.0045	0.1435	−0.0719	0.1301	−0.0197	0.2890	0.1021
5	$\tilde{y}^2$	6.6305	0.1600	6.7711	0.2774	6.7787	0.2803	6.7095	0.4254
6	$\tilde{x}^3$	0.0688	0.0089	−0.0635	0.0066	−0.0855	0.0042	0.1567	0.0100
7	$\tilde{x}^2\tilde{y}$	0.0251	0.0770	0.0941	0.0112	−0.0543	−0.0347	0.0113	−0.0045
8	$\tilde{x}\tilde{y}^2$	−0.0922	−0.0215	0.0010	0.0774	−0.0600	0.0543	−0.0449	0.0378
9	$\tilde{y}^3$	0.0300	0.0824	−0.0325	−0.0003	0.0305	0.0243	−0.0151	0.0544

2015 for a description of the data set) and derived relative proper motions by using the approach described in Massari et al. (2013) and Dalessandro et al. (2013). Only stars in common between the ACS and the WFC3 catalogs and with proper motions $(dx, dy) < 0.1$ mas yr^{-1} (corresponding to 0.002 pixel yr^{-1}) have been selected to build the *master catalog* and derive the GD solution. Such a selection guarantees that the stars in the master catalog are cluster members and are virtually stationary within the uncertainties on proper motion, which correspond to $\Delta v \sim$ 3–4 km s^{-1} with

Table 4
Coefficients of the Third-order Polynomial for each Chip, Representing the Final GD Solution for the *J* Filter

Term(q)	Polynomial	$a_{q,[1]}$	$b_{q,[1]}$	$a_{q,[2]}$	$b_{q,[2]}$	$a_{q,[3]}$	$b_{q,[3]}$	$a_{q,[4]}$	$b_{q,[4]}$
1	$\tilde{x}$	7.3378	−8.0391	−8.2090	−8.1578	−8.5896	5.6014	7.3445	5.3859
2	$\tilde{y}$	−8.5374	−6.8857	−9.5506	7.1074	5.9348	7.4968	6.6005	−5.4962
3	$\tilde{x}^2$	6.6703	0.0347	7.0411	0.0730	6.9823	0.0685	6.7324	−0.0230
4	$\tilde{x}\tilde{y}$	0.1721	0.0946	0.1203	−0.1116	0.1075	−0.0342	0.3678	0.1387
5	$\tilde{y}^2$	6.6176	0.1077	6.7432	0.2616	6.7769	0.2681	6.6951	0.2807
6	$\tilde{x}^3$	0.0220	−0.0157	−0.0464	0.0125	−0.1522	−0.0251	0.2020	−0.0321
7	$\tilde{x}^2\tilde{y}$	−0.0288	0.0233	0.1379	0.0417	−0.1129	−0.0846	0.0102	−0.0558
8	$\tilde{x}\tilde{y}^2$	−0.2149	−0.2188	0.0099	0.1537	−0.1227	0.0069	−0.0205	0.0358
9	$\tilde{y}^3$	0.0112	0.0140	0.0088	−0.0184	0.0092	−0.0102	−0.0273	0.0575

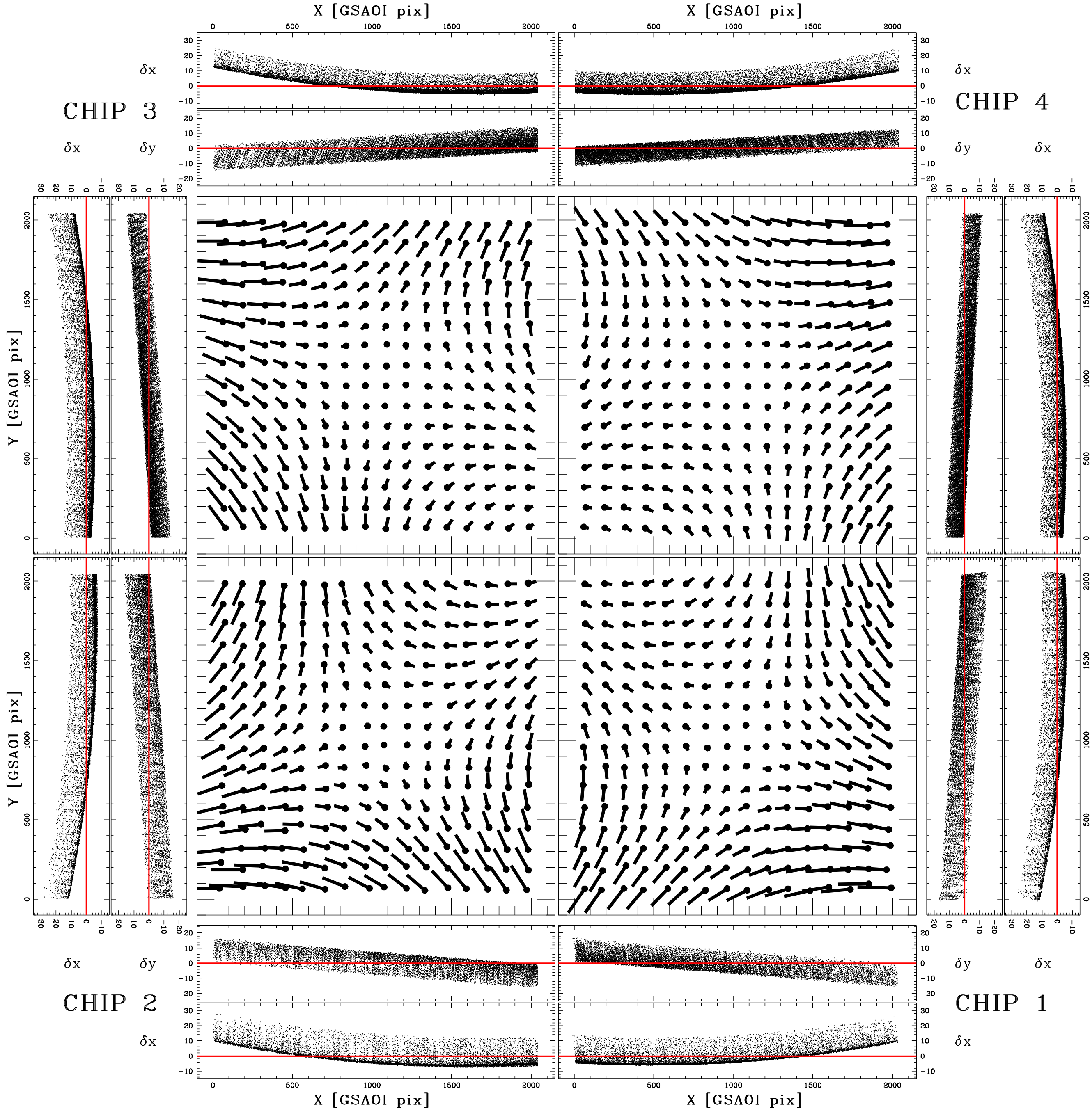

Figure 10. Map of geometric distortion of the four chips of the GSAOI camera, in the K_s filter. Residual vectors are magnified by a factor of 10. For each chip, we also show individual residuals as a function of *x* and *y* axes. The units are GSAOI pixels.

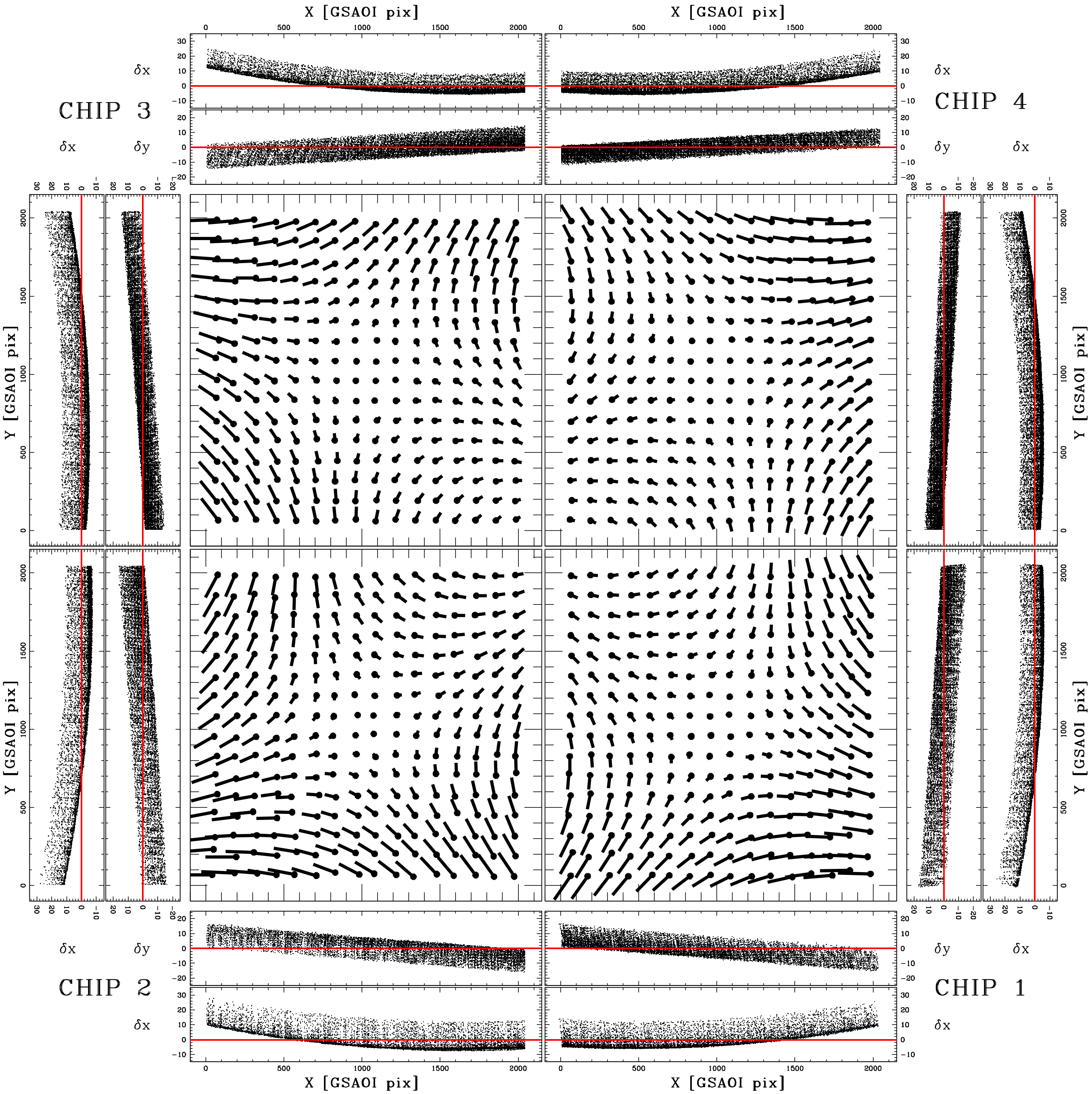

Figure 11. As in Figure 10, but for the J band.

respect to the systemic velocity of the cluster at the distance of NGC 6624. It is important to stress here that the adopted selection corresponds to the typical error on proper motion for well measured stars obtained with similar data sets. Hence more restrictive criteria have no significant impact on the "quality" of the master catalog, but their main effect is on the sample size.

We then matched the master catalog with the GeMS/GSAOI catalog of NGC 6624 described in Saracino et al. (2016) and found ∼7500 stars in common, covering the magnitude range $13 < K_s < 19$. The average crowding in this FOV is ∼13 stars arcsec^{-2} at $K_s < 20.3$ mag. The $(V, V - I)$ and $(K_s, J - K_s)$ color–magnitude diagrams of the stars common to the master catalog and the GeMS/GSAOI catalog of NGC 6624 presented in Saracino et al. (2016) are plotted in Figure 9.

GDs have been computed for each chip, independently, taking as the reference center in each chip the position $(x_0, y_0)_k = (1024, 1024)$ in raw pixel coordinates, where the index $k = 1, 2, 3, 4$ indicates the chip considered. In fact, obtaining a separate solution for each chip, rather than one that uses a common center of the distortion in the FOV, allows better handling of potential individual detector effects.

The main steps of the procedure can be summarized as follows (see also Bellini & Bedin 2009 for more details).

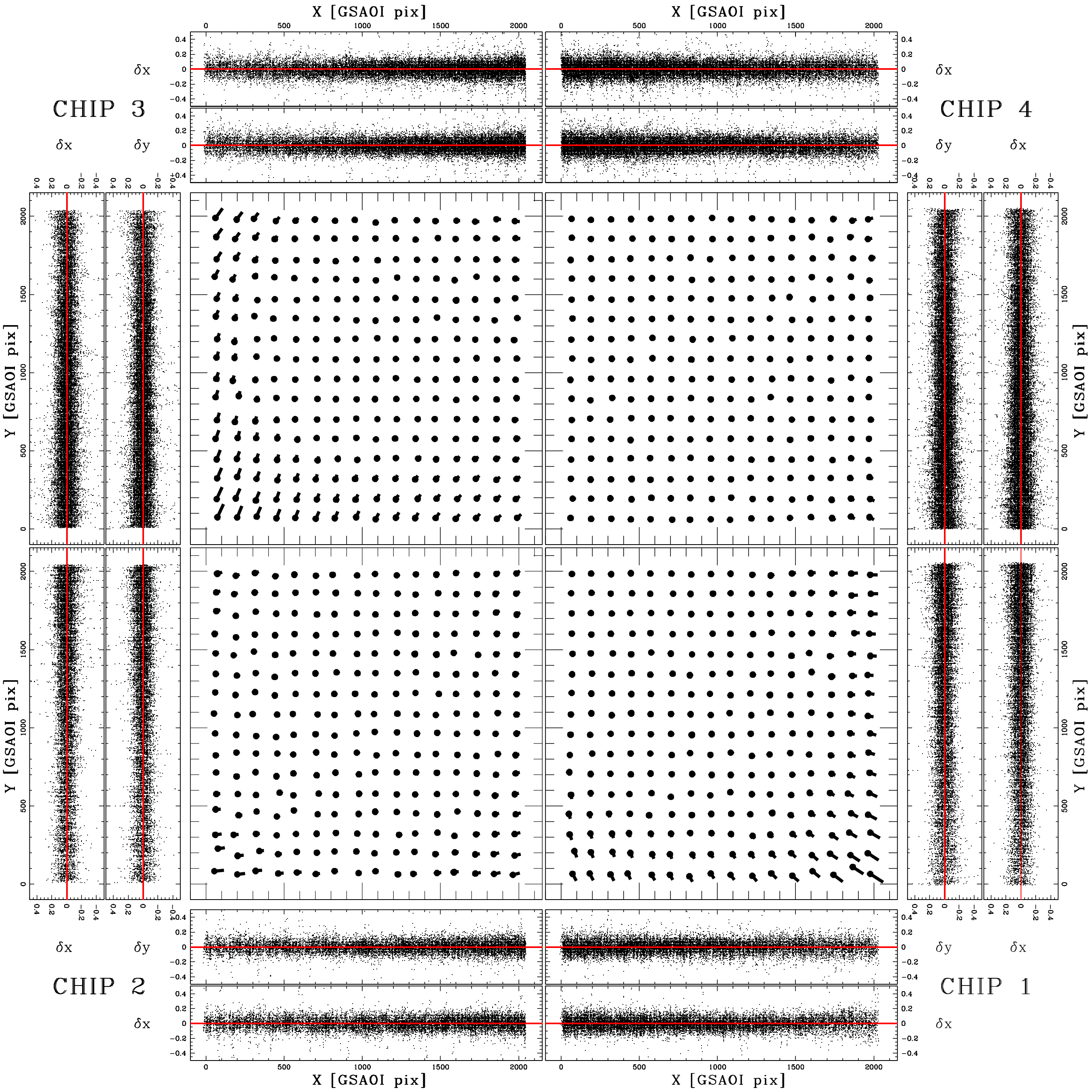

Figure 12. Residual map of the four chips of the GSAOI camera, in the K_s filter, after the GD correction. Residual vectors are magnified by a factor of 5000.

1. We conformally transformed[7] the coordinates of each star i in the master catalog, $(X_i^{\rm master}, Y_i^{\rm master})$, into pixel coordinates of each dithered GeMS/GSAOI image j. We then cross-correlated these nominal positions with those actually measured in each GeMS/GSAOI image j, thus generating pairs of positional residuals:

$$\Delta x_{i,j,k} = x_{i,j,k} - (X_i^{\rm master})^{T_{j,k}}, \quad (1)$$

$$\Delta y_{i,j,k} = y_{i,j,k} - (Y_i^{\rm master})^{T_{j,k}}. \quad (2)$$

   The set of positional residuals $(\Delta x_{i,j,k}, \Delta y_{i,j,k})$ of the stars in the raw images as a function of the $x_{i,j,k}$ and $y_{i,j,k}$ coordinates determines the amount of GD and its spatial distribution in each chip.
2. To create a GD map, we divided each chip (2048 × 2048 pixels) into grids of 16 × 16 cells of 128 × 128 pixels each, in order to have sufficient statistics but also spatial resolution. In each cell we estimated the following parameters[8]: $\bar{x}_{m,k}$, $\bar{y}_{m,k}$, $\overline{\Delta x}_{m,k}$, $\overline{\Delta y}_{m,k}$, and $P_{m,k}$, where $m = 1$–256 is the cell reference number in our grid. $\bar{x}_{m,k}$ and $\bar{y}_{m,k}$ are the average positions of all the stars in each grid cell, $\overline{\Delta x}_{m,k}$ and $\overline{\Delta y}_{m,k}$ the average positional

---

[7] A conformal transformation, also called a Helmert transformation, allows one to switch from one reference system to another, through a change of scale, a rotation, and two rigid shifts along x and y axes, respectively.

[8] The average values of these quantities have been obtained by applying a 3σ rejection.

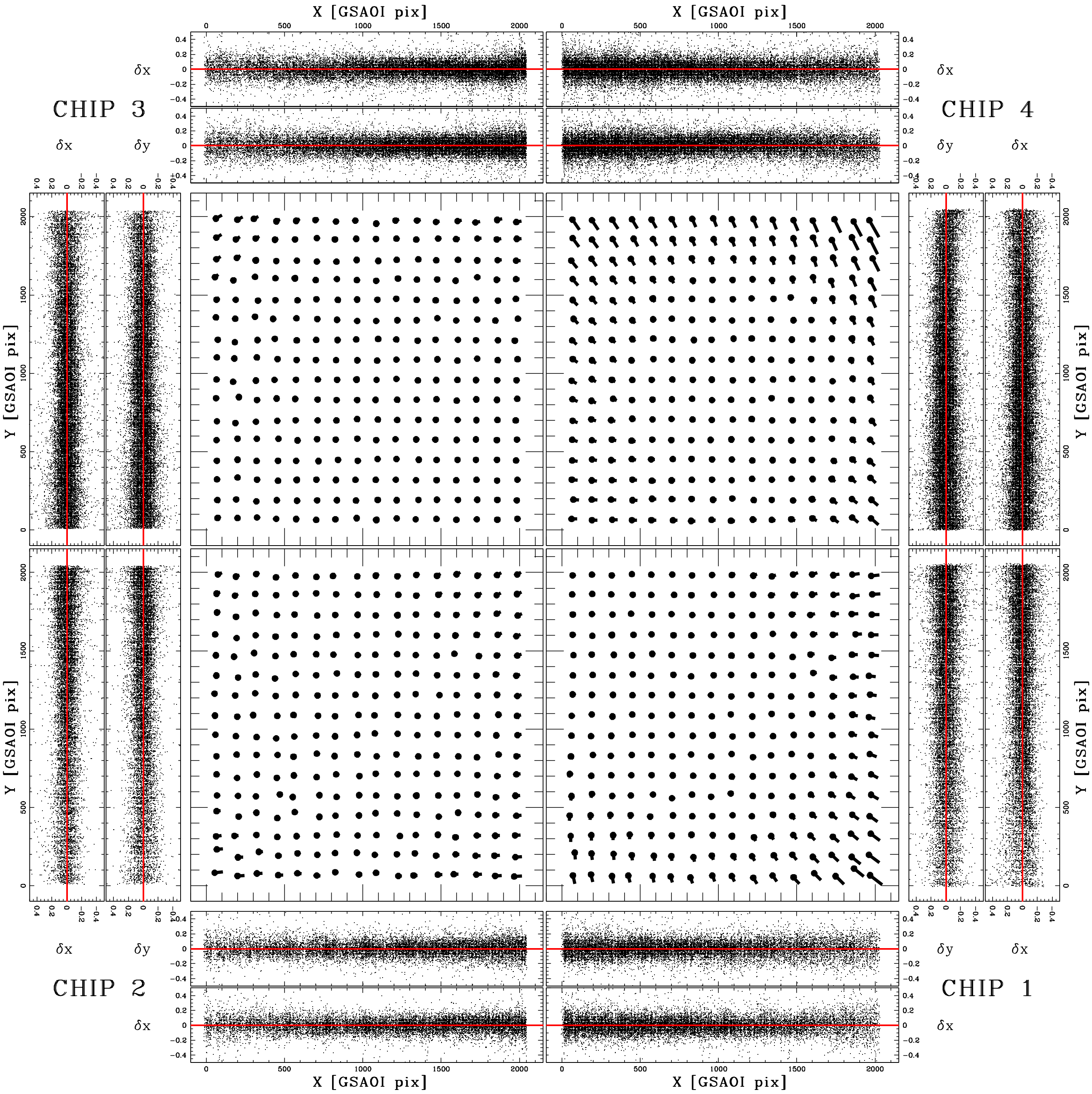

Figure 13. As in Figure 12, but for the *J* band.

residuals, and $P_{m,k}$ indicates the number of stars for each cell.

3. We represented our GD solution with a third-order polynomial (we omitted the indices *i, j*, and *k* for simplicity):

$$\delta x = a_1\tilde{x} + a_2\tilde{y} + a_3\tilde{x}^2 + a_4\tilde{x}\tilde{y} + a_5\tilde{y}^2 + a_6\tilde{x}^3 + a_7\tilde{x}^2\tilde{y} + a_8\tilde{x}\tilde{y}^2 + a_9\tilde{y}^3, \tag{3}$$

$$\delta y = b_1\tilde{x} + b_2\tilde{y} + b_3\tilde{x}^2 + b_4\tilde{x}\tilde{y} + b_5\tilde{y}^2 + b_6\tilde{x}^3 + b_7\tilde{x}^2\tilde{y} + b_8\tilde{x}\tilde{y}^2 + b_9\tilde{y}^3. \tag{4}$$

We verified that a larger number of degrees of freedom did not significantly improve our solution. In this system, $\tilde{x}$ and $\tilde{y}$ indicate the positions of individual stars relative to the central pixel $(x_0, y_0)_k = (1024, 1024)$ of each chip, and $a_{0,k}...a_{9,k}$ and $b_{0,k}...b_{9,k}$ are the 18 coefficients that we need to determine.

To do this, we performed a linear least-squares fit of the 256 data points in each grid cell, which actually means solving a matrix system.

4. After the first GD solution, we determined the distortion-corrected positions $(x^{\rm corr}_{i,j,k}, y^{\rm corr}_{i,j,k})$ as the observed positions $(x_{i,j,k}, y_{i,j,k})$ plus the distortion corrections $(\delta x_{i,j,k}, \delta y_{i,j,k})$:

$$y^{\rm corr}_{i,j,k} = x_{i,j,k} + \delta x(\tilde{x}_{i,j,k}, \tilde{y}_{i,j,k}), \tag{5}$$

$$y_{i,j,k}^{\rm corr} = y_{i,j,k} + \delta y(\tilde{x}_{i,j,k}, \tilde{y}_{i,j,k}). \quad (6)$$

5. The procedure was iterated more than 30 times for a chip by applying only half of the correction at each iteration in order to avoid convergence problems, until the difference in the positional residuals ($\Delta x_{i,j,k}$, $\Delta y_{i,j,k}$ versus $x_{i,j,k}$, $y_{i,j,k}$) from one iteration to the next became negligible (in other words, when $\chi^2_{{\rm iter}N} \approx \chi^2_{{\rm iter}N+1}$).

The coefficients $a_{q,k}$ and $b_{q,k}$ ($q = 1, ..., 9$) of the final GD solution for the four chips are given in Table 3 for the K_s filter, and in Table 4 for the J filter.

Figures 10 and 11 show the GD map and the residual trends of uncorrected star positions for the four chips of the GSAOI camera, in the K_s and J filters, respectively. In both cases, the size of the residual vectors is magnified by a factor of 10. Residual vectors connect the uncorrected average positions within each grid cell to the corrected ones. We also show the overall trend of the positional residuals ($\Delta x_{i,j,k}$ versus $x_{i,j,k}$; $y_{i,j,k}$ and $\Delta y_{i,j,k}$ versus $x_{i,j,k}$; $y_{i,j,k}$). These trends are quite similar/symmetric in the four chips, with a maximum amplitude of ~30 pixels along both the x and y axes.

In Figures 12 and 13 we show the final residuals of the star positions in the K_s and J filters, respectively, after applying our GD solution (residual vectors are magnified by a factor 5000). Our GD solution allowed us to linearize the residual trends in each chip and to reach an astrometric accuracy of about 0.07 pixels, corresponding to ~1.5 mas. In this respect it is worth recalling that, given the selection of proper motion (0.1 mas yr^{-1}) adopted to build the master catalog and the fact that the GeMS/GSAOI images were acquired about seven years after the first *HST* epoch, the total contribution to the final GD error budget due to proper motions can be as large as ~0.7 mas in this case.

As shown by Neichel et al. (2014a), the astrometric accuracy of ground-based instruments in general, and of those assisted by AO systems in particular (e.g., GeMS/GSAOI), depends on a few major factors, namely: (i) the shape and variability of the PSF in the FOV; (ii) the atmospheric conditions (i.e., the seeing at the observing airmass); (iii) the brightness of the three NGSs and their asterism; (iv) the crowding of the observed field; (v) the exposure time.

Because of these important factors, our GD solution based on the observations of NGC 6624 should be further tested on other stellar fields with different crowding, acquired with different atmospheric conditions, asterisms, and exposure times, and with available high-resolution astrometric reference catalogs (likely from *HST* imaging). While the general formal solution would likely be still valid in a first-order approximation, data sets obtained under different observing conditions may yield different coefficients. Unfortunately, our observations of Liller 1 cannot be used for such a test since no astrometric reference catalog based on high-resolution data is available for this very reddened cluster.

However, we have verified that the GD residuals (after correction) obtained for NGC 6624 are quantitatively compatible with those obtained for NGC 6681 (Massari et al. 2016) observed under different seeing conditions and NGS asterism. Our results are also qualitatively consistent with those obtained by Ammons et al. (2016) for the globular cluster NGC 1851, although a more quantitative comparison is not possible because the authors do not provide enough details.

It is also important to stress that the analysis described in this section has a general relevance, since it provides the mathematical formalism to correct for GDs and it can thus be effectively applied to any photometric data set.

5. CONCLUSIONS

The PSF tests performed on the GeMS/GSAOI J and K_s images of the central region of two high-density globular clusters have provided very interesting results.

The ground-based MCAO-assisted imager GeMS/GSAOI at Gemini South observatory provides a unique and powerful facility to derive accurate stellar photometry at a spatial resolution near the diffraction limit, at least in the K_s band where AO correction is more efficient. A uniform (at a level of ~10%) PSF over an FOV of 1′–2′ with up to 50%–60% EE within 2 FWHM can be obtained in good seeing conditions. This performance is comparable with those delivered by *HST* imagers at optical wavelengths.

Following the same strategy adopted for other imagers on board *HST* and for wide-field ground-based cameras, we were also able to compute GDs for GeMS/GSAOI and provide corrected images with an astrometric accuracy of ~1.5 mas in a stellar field with a crowding of ~13 stars arcsec^{-2} at $K_s \leqslant 20.3$ mag, thus demonstrating that a ground-based MCAO-assisted imager at an 8 m class telescope can provide accurate NIR photometry and absolute astrometry for studies of proper motion in very dense stellar fields, in some cases outperforming *HST*'s capability as a result of the higher spatial resolution. *HST* with its ACS and WFC3 imagers remains almost unique in providing photometry of the faintest stars in less crowded regions.

Looking at future facilities, complementarity can be foreseen also with the *James Webb Space Telescope* (*JWST*), which will provide the deepest photometry in the NIR over a FOV of a few arcminutes at about the same spatial resolution as *HST*, and with ground-based MCAO-assisted imagers at 20–40 m class telescopes, which will provide significantly higher spatial resolution at the same wavelengths as *JWST* but over a smaller FOV.

We thank the anonymous referee for his/her useful comments and suggestions. E.D. and S.S. thank Andrea Bellini and Benoit Neichel for useful discussions and suggestions. L.O. acknowledges the PRIN-INAF 2014 CRA 1.05.01.94.11: “Probing the internal dynamics of globular clusters. The first comprehensive radial mapping of individual star kinematics with the new generation of multi-object spectrographs” (PI: L. Origlia). D.G., S.V., and R.E.C. gratefully acknowledge support from the Chilean BASAL Centro de Excelencia en Astrofísica y Tecnologías Afines (CATA) grant PFB-06/2007. R.E.C. also acknowledges funding from Gemini-CONICYT for Project 32140007.

Software: Multi-Strehl Meter (Marchetti et al. 2006).

REFERENCES

Ammons, S. M., Garcia, E. V., Salama, M., et al. 2016, Proc. SPIE, 9909, 99095T

Anderson, J., Bedin, L. R., Piotto, G., Yadav, R. S., & Bellini, A. 2006, A&A, 454, 1029

Anderson, J., & King, I. R. 2003, PASP, 115, 113

Beckers, J. M. 1988, in European Southern Observatory Conf. and Workshop Proc. 30, ed. M.-H. Ulrich, 693

Bellini, A., Anderson, J., & Bedin, L. R. 2011, PASP, 123, 622

Bellini, A., & Bedin, L. R. 2009, PASP, 121, 1419
Bellini, A., & Bedin, L. R. 2010, A&A, 517, A34
Bellini, A., Piotto, G., Bedin, L. R., et al. 2009, A&A, 493, 959
Bellini, A., Vesperini, E., Piotto, G., et al. 2015, ApJL, 810, L13
Bono, G., Stetson, P. B., VandenBerg, D. A., et al. 2010, ApJL, 708, L74
Dalessandro, E., Ferraro, F. R., Massari, D., et al. 2013, ApJ, 778, 135
Ellerbroek, B. L., Pompea, S. M., Robertson, D. J., & Mountain, C. M. 1994, Proc. SPIE, 2201, 421
Ferraro, F. R., Dalessandro, E., Mucciarelli, A., et al. 2009, Natur, 462, 483
Johnston, D. C., & Welsh, B. M. 1994, JOSAA, 11, 394
Le Louarn, M. 2002, MNRAS, 334, 865
Libralato, M., Bellini, A., Bedin, L. R., et al. 2014, A&A, 563, A80
Libralato, M., Bellini, A., Bedin, L. R., et al. 2015, MNRAS, 450, 1664
Marchetti, E., Brast, R., Delabre, B., et al. 2006, Proc. SPIE, 6272, 62720O
Marchetti, E., Brast, R., Delabre, B., et al. 2007, Msngr, 129, 8
Massari, D., Bellini, A., Ferraro, F. R., et al. 2013, ApJ, 779, 81
Massari, D., Fiorentino, G., McConnachie, A., et al. 2016, arXiv:1609.05923
Meurer, G. R., Lindler, D. J., Blakeslee, J., et al. 2003, Proc. SPIE, 4854, 507
Moretti, A., Piotto, G., Arcidiacono, C., et al. 2009, A&A, 493, 539
Neichel, B., Lu, J. R., Rigaut, F., et al. 2014, MNRAS, 445, 500
Neichel, B., Rigaut, F., Vidal, F., et al. 2014b, MNRAS, 440, 1002
Ortolani, S., Barbuy, B., Momany, Y., et al. 2011, ApJ, 737, 31
Piotto, G., Milone, A. P., Bedin, L. R., et al. 2015, AJ, 149, 91
Richer, H. B., Heyl, J., Anderson, J., et al. 2013, ApJL, 771, L15
Rigaut, F., Neichel, B., Boccas, M., et al. 2012, Proc. SPIE, 8447, 84470I
Rigaut, F., Neichel, B., Boccas, M., et al. 2014, MNRAS, 437, 2361
Saracino, S., Dalessandro, E., Ferraro, F. R., et al. 2015, ApJ, 806, 152
Saracino, S., Dalessandro, E., Ferraro, F. R., et al. 2016, ApJ, 832, 48
Sarajedini, A., Bedin, L. R., Chaboyer, B., et al. 2007, AJ, 133, 1658
Sirianni, M., Jee, M. J., Benítez, N., et al. 2005, PASP, 117, 1049
Vidal, F., Neichel, B., Rigaut, F., et al. 2013, in Proc. Third AO4ELT Conf., ed. S. Esposito & L. Fini, 46
Watkins, L. L., van der Marel, R. P., Bellini, A., & Anderson, J. 2015, ApJ, 803, 29
Yadav, R. K. S., Kumar, B., Subramaniam, A., Sagar, R., & Mathew, B. 2008, MNRAS, 390, 985